ELSEVIER

Journal of Membrane Science 157 (1999) 13–34

journal of MEMBRANE SCIENCE

An unsteady-state model to predict concentration polarization in commercial spiral wound membranes

K. Madireddi[a], R.B. Babcock[b], B. Levine[c], J.H. Kim[d], M.K. Stenstrom[e,*]

[a]*EMC Corp., 3961 Kamden Way, Las Vegas, NV 89119, USA*
[b]*Department of Civil Engineering, University of Hawaii, 2540 Dole Street, Holmes Hall 383, Honolulu, HI 96822, USA*
[c]*Center of International Research for Water and Environment (CIRSEE)/Lyonnaise Des Eaux, 78230 Le Pecq, France*
[d]*Environmental and Biological Engineering Division, Kangwon National University, 192-1 Hyojadong, Chunchon Kangwondo 200-701, South Korea*
[e]*Department of Civil and Environmental Engineering, University of California, 4173 Engr I, Los Angeles, CA 90095-1953, USA*

Received 20 June 1998; received in revised form 11 August 1998; accepted 19 October 1998

Abstract

A comprehensive finite difference model is developed and presented to predict concentration polarization (CP) in commercial spiral wound membranes. The model was developed by solving the non-conservative mass balance equation in the feed channel employing fluid flow profiles based on feed spacer mixing. Both ideal membranes with complete solute rejection characteristics and non-ideal membranes were considered. The model predicts CP for low, moderate as well as high solvent recovery up to 90%. The model was tested for numerical stability and convergence, and subsequently applied to generate CP and permeate flow loss information for a range of feed and operating conditions. The model results were verified experimentally on 1.89×10^{-4} m^3/s pilot-scale spiral wound reverse osmosis (RO) unit. Since flow loss in membranes is a dynamic phenomenon, it is anticipated that the model will be an appropriate choice for further work on predicting long-term permeate flow loss from membrane fouling.

Keywords: Concentration polarization; Modeling; Spiral wound membranes

1. Introduction

Membrane separation processes such as RO and ultrafiltration (UF) have gained considerable importance because they offer superior treatment at relatively modest capital and operating costs [1,2]. The processes remove a wide range of contaminants present in untreated water, municipal and industrial wastewater discharges such as suspended and dissolved solids, organic matter, heavy metals, bacteria and viruses [3]. In spite of the above advantages, the progress of membrane implementation at full-scale has been restricted because of two principal problems commonly encountered during operation: concentration polarization (CP) and fouling. CP refers to an increase in concentration of contaminants (solutes) near the membrane surface that create additional resistance to separation. Thus, CP increases operating costs while also adversely affecting product water

*Corresponding author. Tel.: +1-310-825-1408; fax: +1-310-206-5476; e-mail: stenstro@stanley.seas.ucla.edu

0376-7388/99/$ – see front matter
PII: S0376-7388(98)00340-8

quality. Membrane fouling refers to the long-term decline in the permeate flux from prolonged operation. Fouling is a complex phenomenon with a number of influencing factors such as membrane pore plugging, chemical degradation and bacterial growth [4]. Depending on the size of the system, fouling manifests over a long period ranging from a few 100 h to several 1000 h of operation. It is acknowledged that CP generally increases fouling, because it increases the concentration of contaminants such as bacteria, organic and inorganic material near the membrane surface, which aggravate fouling.

Concentration polarization was previously studied from a theoretical view so that its effects could be included in membrane design and operation. Most of these studies centered on solving the solute mass balance equation with appropriate fluid velocity profiles using various numerical methods [5]. Most of these models assume steady-state conditions and/or deal with simplified membrane systems operating at low product water recoveries. The present study was undertaken to model CP for commercial membrane units operating at moderate to high recoveries (50–90%). In addition, the initial transient state performance of the unit is also studied by taking into account the non-steady-state term in the mass balance equation. Such a time-dependent analysis can include the effects of long-term decline in product water flow due to fouling and membrane degradation.

Two types of membrane modules, spiral wound and hollow-fiber configurations, dominate the desalination and water treatment systems. The main advantage of these modules is high membrane packing density, which allows for compact design and easy installation of the units. Hollow-fiber membranes are more susceptible to fouling from particulate and colloidal matter and therefore widely used in water treatment. For wastewater reclamation applications, spiral wound membranes which are relatively more tolerant to these contaminants are more appropriate. In this paper, a transient model is developed to analyze and predict CP for a spiral wound membrane system.

2. Model development

Fig. 1(a) represents a spiral wound membrane that is unwound; the flow within the module which approximates flow in a channel with two porous walls if spiraling effects are ignored. The flow balance equations are represented by the expanded Navier–Stokes equations as follows [3]:

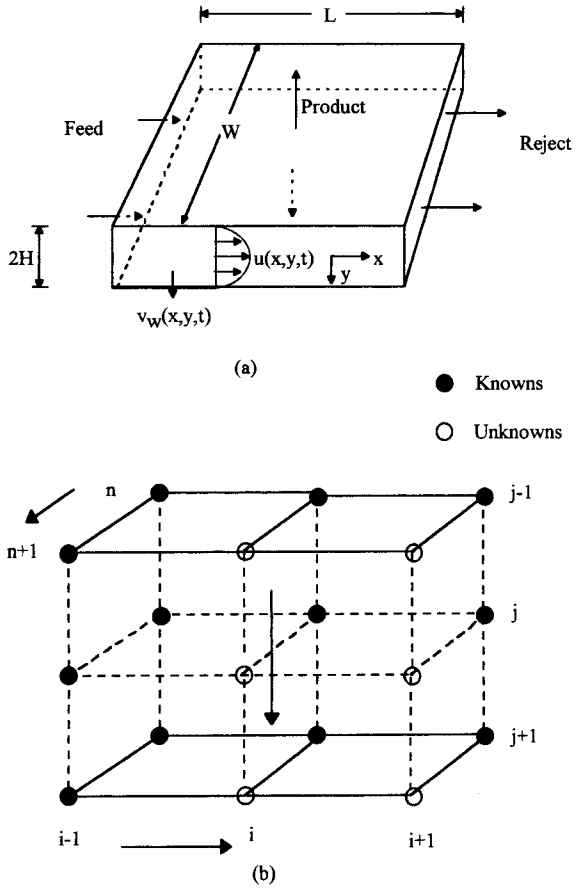

Fig. 1. (a) Flow in channel with two porous walls (spiral wound module) and (b) graphical representatin of the finite difference (FD) solution.

$$x\text{-momentum}: \quad \frac{\partial u}{\partial t} + u\frac{\partial u}{\partial x} + v\frac{\partial u}{\partial y} = -\frac{1}{\rho}\frac{\partial P}{\partial x} + \nu\left(\frac{\partial^2 u}{\partial x^2} + \frac{\partial^2 u}{\partial y^2}\right), \tag{1}$$

$$y\text{-momentum}: \quad \frac{\partial v}{\partial t} + u\frac{\partial v}{\partial x} + v\frac{\partial v}{\partial y} = -\frac{1}{\rho}\frac{\partial P}{\partial x} + \nu\left(\frac{\partial^2 v}{\partial x^2} + \frac{\partial^2 v}{\partial y^2}\right), \tag{2}$$

$$\text{Continuity}: \quad \frac{\partial u}{\partial x}+\frac{\partial v}{\partial y}=0, \tag{3}$$

where u and v are the axial and transverse (lateral) velocities, P is the pressure, ρ the density and ν is the kinematic viscosity. The mass balance equation is written in its conservative form as follows:

$$\frac{\partial c}{\partial t}=D_s\frac{\partial^2 c}{\partial y^2}-\frac{\partial u\,c}{\partial x}-\frac{\partial v\,c}{\partial y}, \tag{4}$$

where D_s is the solute diffusivity and c is the solute concentration. Substituting (3) into (4) leads to the mass balance equation in its non-conservative form as

$$\frac{\partial c}{\partial t}=D_s\frac{\partial^2 c}{\partial y^2}-u\frac{\partial c}{\partial x}-v\frac{\partial c}{\partial y}. \tag{5}$$

Most of the available models solve Eq. (4) or Eq. (5) in their steady-state form along with appropriate expressions for the velocities u and v. In this paper, this methodology is preserved but the time dependent term is included during numerical model development. Available expressions for u and v are based on analytical methods applied to solve the flow balance equations in channels with two porous walls (Table 1). The second term on the right-hand side of Eqs. (6a), (6b) and (7) is generally neglected because of its lower magnitude compared to the first term. For spiral wound membranes, the presence of feed spacers that promote mixing and turbulence distort the laminar profile of the axial flow. This distortion has been previously studied in detail, and is presented in Eqs. (8a) and (8b) as a function of a mixing parameter m [6]. For low values of m (less than 1), the axial profile resembles the parabolic shape laminar flow while for high values of m (greater than 100), the profile resembles the uniform shape of completely mixed flow.

Eq. (5) was scaled using appropriate scaling factors (see Section 6) to yield a modified mass balance equation in its non-dimensional form as

$$\frac{\partial C}{\partial T}=D\frac{\partial^2 C}{\partial Y^2}-V\frac{\partial C}{\partial Y}-U\frac{\partial C}{\partial X}. \tag{9}$$

The initial and boundary conditions are given as

$$C=0 \quad \text{at } T=0, \tag{10a}$$

$$C=1 \quad \text{at } X=0, \tag{10b}$$

$$\frac{\partial C}{\partial Y}=0 \quad \text{at } Y=0, \tag{10c}$$

$$D\frac{\partial C}{\partial Y}=V_w C_w-V_p C_p \quad \text{at } Y=1. \tag{10d}$$

Eq. (10b) represents concentration at the inlet, and is equal to 1 in the absence of recycle. During recycle mode, a portion of the reject stream is diverted and mixed with the feed stream. For recycle>0, the inlet

Table 1
Expressions for axial and lateral velocities in channels with two porous walls

(1) Laminar flow [11]

$$u(x,y)=\frac{3}{2}u_{avg}(x)\left(1-\left(\frac{y}{H}\right)^2\right)\left[1-\frac{Re_y}{420}\left(2-7\left(\frac{y}{H}\right)^{Y_2}-7\left(\frac{y}{H}\right)^4\right)\right], \tag{6a}$$

$$u_{avg}(x)=u_{avg}(0)-\frac{v_w x}{H}, \tag{6b}$$

$$\frac{v(y)}{v_w}=\frac{y}{2H}\left(3-\left(\frac{y}{H}\right)^2\right)-\frac{Re_y}{280}\frac{y}{H}\left(2-3\left(\frac{y}{H}\right)^2+\left(\frac{y}{H}\right)^6\right), \tag{7}$$

(2) Spiral wound flow [10]

$$u(x,y)=\frac{dP}{dx}\frac{h^2}{\eta m^2}\left(1-\frac{v_w x}{u_0 h}\right)\left\{(m+1)\ln\left[m\left(1-\frac{y}{h}\right)+1\right]-m\left(1-\frac{y}{h}\right)\right\}, \tag{8a}$$

where

$$m=2.1\times 10^5\,[n_s\,(t_s-d_s)]^{2.4}\left(\frac{1-\epsilon}{\epsilon^3}\right)^{0.8}. \tag{8b}$$

Note: Expression for $v(y)$ remains unchanged.

boundary condition is appropriately modified into

$$C = \frac{1 + R_c C_R}{1 + R_c}, \tag{10e}$$

where R_c is the recycle ratio, and C_R is the scaled recycle solute concentration, which is a function of time. Hence, the inlet boundary condition is time-dependent boundary condition that develops as recycle solute concentration increases from an initial zero (if the model run is started assuming steady-state clean water conditions initially) to a finite positive value. Eq. (10a) represents initial clean water operating conditions without CP, while Eqs. (10c) and (10d) represent boundary conditions at the axial center-line (symmetry) and membrane wall (CP), respectively.

The velocity profiles were also similarly scaled to obtain

$$U(X,Y,T) = U_{avg}(X,T)\,\frac{3}{2}\left(1 - Y^2\right), \tag{11}$$

$$V(X,Y,T) = V_w(X,T)\,\frac{Y}{2}\left(3 - Y^2\right), \tag{12}$$

where

$$U_{avg}(X,T) = 1 - \int_0^X V_w(X,T)\,dX \tag{13}$$

Eqs. (11) and (12) represent profiles for laminar flow in porous channels; for spiral wound flow, lateral profile remains the same while the axial profile assumes

$$U(X,Y,T) = U_{avg}(X,T) \times \frac{\{(m+1)\ln[m(1-Y)+1] - m(1-Y)\}}{(m+1)^2\ln(m+1) - 1.5\,m^2 - m}. \tag{14}$$

For $m \to \infty$, Eq. (14) represents completely mixed flow as

$$U(X,Y,T) = U_{avg}(X,T). \tag{15}$$

In addition, the following axial pressure drop equation was used:

$$P(X) = P(0) - \Delta P_{ax}\,X. \tag{16}$$

In this study, the maximum axial pressure drop (ΔP_{ax}) was observed to be 10% of the inlet pressure in all the experiments; therefore, this value was substituted in Eq. (16) to compute $P(X)$. This approximation was employed instead of calculating pressure drop variation spatially and in time using the fluid flow equation. The approximation reduced overall model calculation times as substantial number of additional iterations were required to allow the pressure drop to converge to a stable value at each axial step. The approximation also reduced problems associated with model stability and accuracy.

Finally, a membrane permeation flux equation based on the osmotic model was used to obtain membrane permeation velocity:

$$v_w(x,t) = A(\Delta P(x,t) - \Delta\Pi(x,t)), \tag{17}$$

where A is the membrane permeability, and ΔP and $\Delta\Pi$ are the applied pressure and the induced osmotic back pressure. The corresponding scaled membrane permeation velocity is denoted by V_w. The osmotic pressure is described as a linear function of the solute concentration as

$$\Pi = K_{osm}c, \tag{18}$$

where K_{osm} is the osmotic pressure coefficient.

A finite difference (FD) formulation was employed to solve Eq. (9) and the supporting fluid flow and membrane permeation equations; these included a space averaged centered-difference analog for time derivative, a time averaged centered-difference analog for the axial derivative, and modified Crank–Nicholson analogs for the transverse derivatives. The analogs were written at the center of the grid unit and the subscripts i, j and n refer to axial, transverse and time coordinates as shown in Fig. 1(b).

$$\left.\frac{\partial C}{\partial T}\right|_{i-\frac{1}{2},j,n+\frac{1}{2}} = \frac{1}{2}\left\{\frac{C_{i-1,j,n+1} - C_{i-1,j,n}}{\Delta T} + \frac{C_{i,j,n+1} - C_{i,j,n}}{\Delta T}\right\}, \tag{19}$$

$$U\frac{\partial C}{\partial X} = U_{i-\frac{1}{2},j,n+\frac{1}{2}}\left.\frac{\partial C}{\partial X}\right|_{i-\frac{1}{2},j,n+\frac{1}{2}}, \tag{20a}$$

$$\left.\frac{\partial C}{\partial X}\right|_{i-\frac{1}{2},j,n+\frac{1}{2}} = \frac{1}{2}\left\{\frac{C_{i,j,n} - C_{i-1,j,n}}{\Delta X} + \frac{C_{i,j,n+1} - C_{i-1,j,n+1}}{\Delta X}\right\}, \tag{20b}$$

$$V\frac{\partial C}{\partial Y} = V_{i-\frac{1}{2},j,n+\frac{1}{2}}\left.\frac{\partial C}{\partial Y}\right|_{i-\frac{1}{2},j,n+\frac{1}{2}}, \tag{21a}$$

$$= \left.\frac{\partial C}{\partial Y}\right|_{i-\frac{1}{2},j,n+\frac{1}{2}} = \frac{1}{4}\left\{\frac{C_{i-1,j,n+1} - C_{i-1,j-1,n}}{2\Delta Y} + \frac{C_{i-1,j+1,n+1} - C_{i-1,j-1,n+1}}{2\Delta Y} + \frac{C_{i,j+1,n} - C_{i,j-1,n}}{2\Delta Y} + \frac{\underline{C}_{i,j+1,n+1} - \underline{C}_{i,j,n+1}}{2\Delta Y}\right\}, \tag{21b}$$

$$D\frac{\partial^2 C}{\partial Y^2} = D\frac{1}{4}\left\{\frac{C_{i-1,j+1,n} - 2C_{i-1,j,n} + C_{i-1,j-1,n}}{\Delta Y^2} + \frac{C_{i-1,j+1,n+1} - 2C_{i-1,j,n+1} + C_{i-1,j-1,n+1}}{\Delta Y^2} + \frac{C_{i,j+1,n} - 2C_{i,j,n} + C_{i,j-1,n}}{\Delta Y^2} + \frac{\underline{C}_{i,j+1,n+1} - \underline{2C}_{i,j,n+1} + \underline{C}_{i,j-1,n+1}}{\Delta Y^2}\right\}. \tag{22}$$

The axial and transverse velocities at the center were calculated employing a four-point average method as follows:

$$U_{i-\frac{1}{2},j,n+\frac{1}{2}} = \frac{1}{4}\left\{U_{i-1,j,n} + U_{i,j,n} + U_{i-1,j,n+1} + \underline{U}_{i,j,n+1}\right\}, \tag{23}$$

$$V_{i-\frac{1}{2},j,n+\frac{1}{2}} = \frac{1}{4}\left\{V_{i-1,j,n} + V_{i,j,n} + V_{i-1,j,n+1} + \underline{V}_{i,j,n+1}\right\}. \tag{24}$$

All the known and unknown terms (underlined) in Eq. (9) were rearranged to create a canonical form, as follows:

$$a_j C_{i,j-1,n+1} + b_j C_{i,j,n+1} + d_j C_{i,j,n+1} = e_j, \tag{25}$$

where a_j, b_j and d_j are coefficients that involve constants and velocities as computed using Eqs. (23) and (24) while e_j is the term that involves constants, known concentrations and velocities. It should be noted that the last terms in Eqs. (23) and (24) are unknowns that depend on solute concentration at the membrane surface at the new time level; therefore, an iterative technique is required for solution. Eq. (25) was solved using the tri-diagonal Thomas algorithm after incorporating the necessary boundary conditions [7].

As the permeation recoveries were relatively significant (above 50%), the spiral wound unit was divided into K equal elements axially; the values ranged from 1 to 10 depending on the size of the module and the initial operating recovery. Each element was individually scaled in the same manner as the first element; however, element characteristics and initial axial velocities at each inlet were employed for scaling. The overall effect was to solve the mass balance equation successively for K elements with low recoveries in contrast to solving the mass balance as a single unit operating at high recovery. This procedure increased the computation time but considerably increased numerical stability and the overall accuracy. The computation was started at the inlet to the first element (K=1). The solute concentration values at n=1 (old time level) were computed for all values of i and j from the initial condition; simultaneously, the concentration values at n=2 (new time level) were computed for i=1 and all values of j from the axial boundary condition at the inlet. Thus, the concentrations are known for three columns shown in Fig. 1(b) marked by dark circles; the last column consists of terms with unknown solute concentrations and velocities, and therefore equations analogous to Eq. (25) are written for all transverse grid points from j=1 to $j=j_{\max}$ based on solute mass balance, and arranged tri-diagonally. The first term of the first equation ($a\,C_{i,1,\,n+1}$) and the third term of the last equation ($d\,C_{i,j\max,n+1}$) are eliminated employing the two transverse boundary conditions at Y=0 and Y=1. The remaining equations are conveniently solved for concentration values employing the Thomas algorithm.

The velocities that are required to compute the coefficients a, b and d are based on four-point average as in Eqs. (23) and (24); these velocities are dependent on solute concentration at the old and new time levels. In order to remove this non-linearity, an iterative technique is employed; the velocities at the new time level and at i=2 are assumed to be equal to old time level values for the first guess, the coefficients a, b and d are then computed and Eq. (25) is solved for all values of j at i=2. The new solute concentration is used to compute the osmotic pressure from Eq. (18), and the membrane permeation velocity at the new time level from Eq. (17); the new value is then substituted in the transverse velocity profile to obtain values for all j. The axial velocities at the new time level are subsequently computed from an incremental flow balance. These values are substituted in Eq. (25), and the procedure is repeated to convergence. For

this study, a convergence criterion of 0.5% was chosen for old and new values of the permeation velocity.

The solution progresses through successive axial increments until all the grid concentrations were computed at the new time level for the first element (K=1). Simultaneously, the permeation velocities were computed and integrated axially to yield the permeate flow for this element at the new time level. The calculations proceed through successive elements (K=2,3,...) until all the elements are solved for solute concentrations at the new time level. The permeation velocities in individual elements were computed as before and integrated to yield permeate flows for the elements; the permeate flows for each element are summed to yield the total permeate flow from the module at the new time level. Calculations proceed through successive time steps until steady-state is attained.

The model was also extended to include recycle flow; it was assumed that at the start of each run, the fluid flow (pure water) was at steady-state with constant recycle. In this case, the introduction of solute in the feed flow does not appear as a constant boundary condition at the inlet; it starts at a numerically lower value than the feed concentration because of recycle mixing. As time progresses, the recycle solute concentration increases which increases the inlet feed concentration to a constant value at steady-state. However, this did not disturb the sequence of calculations in the numerical model.

A computer program was written in FORTRAN 77 for the model described above. After analyzing the model for stability, 10 transverse grid elements were found be sufficient; a time step equal to one-two hundredth of the nominal residence time was chosen for each element in the module. As the CDE was hyperbolic in the axial direction, the same number of axial steps were also chosen; a characteristics averaging scheme is more suitable for hyperbolic equations where the axial grid steps are taken in proportion the axial velocity propagation. However, the axial velocities varied from the inlet to exit section of each element and also in the transverse direction making it difficult for characteristics averaging to be successfully employed. Some error from numerical dispersion was unavoidable because of the presence of the non-uniform velocity profiles. However, in the model, the division of the spiral wound module into several axial elements gave the effect of solving low recovery problems successively and thus decreased the magnitude of the numerical error in the axial direction. The program was run on an IBM RISC 6000/550E power station. For a typical transient run from start-up to steady-state involving 500 to 1000 time steps, approximately 1 min of computing time was required; this time could be further reduced if larger time steps are taken as the problem reaches steady-state. The rapid solution allowed the model to predict behavior for a range of operating pressures, feed concentrations and ambient conditions.

3. Experimental

3.1. Determination of A, D_s and K_{osm}

The permeability A values were evaluated from pure water permeation experiments conducted on the membrane at different operating pressures and ambient temperatures. Eq. (17) was used to relate permeation flux (m/s) with the average operating pressure (KPa) for two different feed flow rates, and subsequently used to compute A. The computed A values were plotted against ambient temperature as shown in Fig. 2(a). This information can also be alternatively obtained from the membrane manufacturer. NaCl–water system was used to verify model predictions. There is negligible variation in the value of D_s for the range of NaCl concentrations from 0 to 1.6 molar (M) [8]; hence, a value of 1.61×10^{-9} m^2/s that represents molecular diffusivity was used in all model runs. The effect of NaCl concentration on osmotic pressure at different ambient temperatures has also been documented [8]. The osmotic pressure data were plotted versus NaCl concentrations in the range of 0.1–1.0 M at different temperatures; K_{osm} was computed as the slope of these lines (Fig. 2(b)).

3.2. Pilot-scale experimental set-up

A pilot-scale RO unit that was operated in Lake Arrowhead, CA, as a part of a reclamation study, was used to verify model results experimentally [9]. The unit was purchased from DESAL, and consisted of three spiral wound RO elements 1.0 m (40 in.) in length and 0.1 m (4 in.) in diameter placed in series

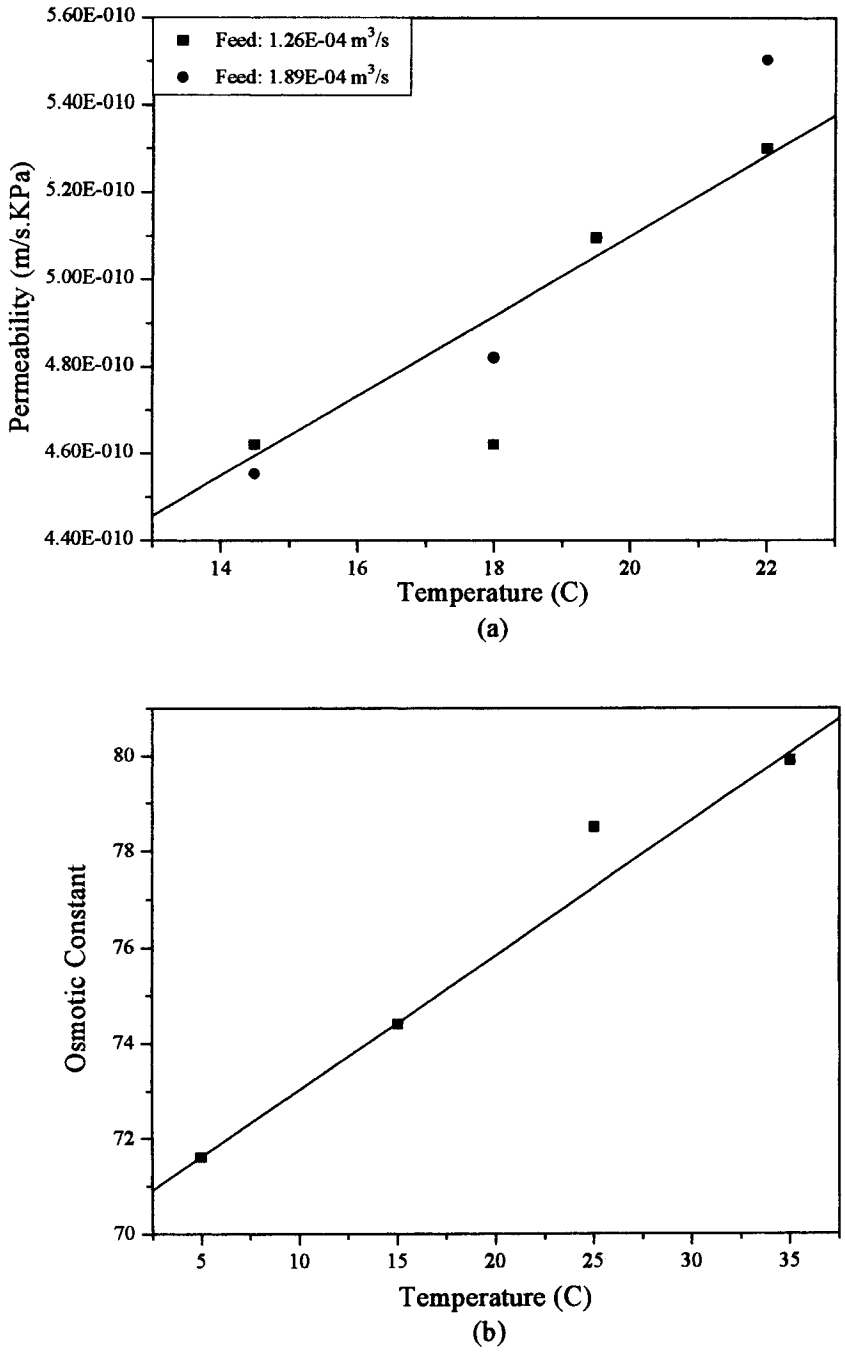

Fig. 2. (a) Permeability data on membranes used in this study and (b) osmotic constant K_{osm} (KPa m^3/kg) versus temperature based on data from [8].

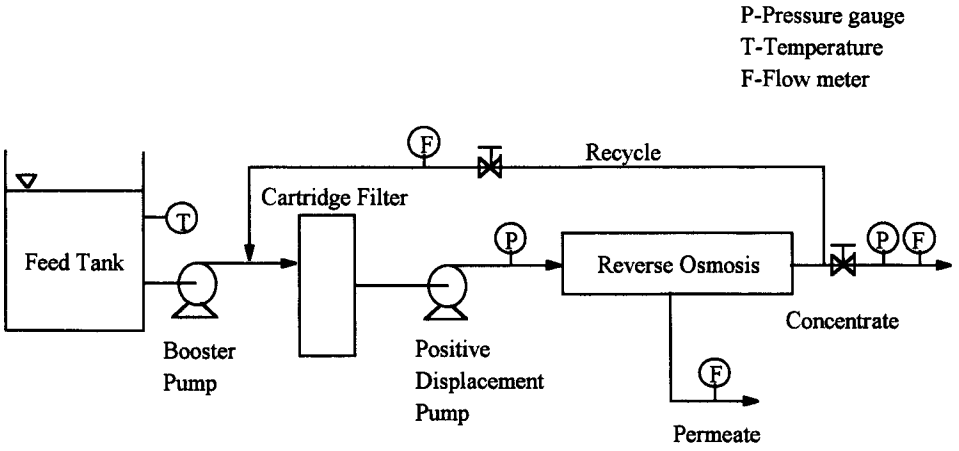

Fig. 3. Schematic of the pilot-scale experimental RO unit.

in a single module, and mounted on a transportable skid with two feed pumps, cartridge filters, and stainless steel piping (Fig. 3). A centrifugal booster pump was used to push the flow across two one-micron cartridge filters to remove particulate matter while a positive displacement pump was used to develop dynamic head up to 2070 KPa (300 psi) necessary for RO separation. The design product flow ranged from 1.67×10^{-4} to 2.5×10^{-4} m/s (i.e., 10–15 l/min) for permeate recoveries between 50% and 95%. The feed to the unit was NaCl–water solutions prepared from "pure water" with electric conductivity (EC) less than 10 μmho/cm, and non-iodized salt. The pure water was RO-treated tap water produced in batches of 1.0 m^3 for each experiment. This procedure was used instead of using purchasing laboratory grade DI water because of the unusually large quantity (1.0 m^3) that was required to prepare the feed solution for each experimental run. As this procedure for producing pure water slightly fouled the membranes; the permeability data were collected on these lightly fouled membranes. The adjusted value of A includes any fouling and/or degradation effects during the production of the pure water.

Parameters such as fluid temperature, operating pressures and fluid concentrations were measured during and at the end of each experimental run to facilitate both transient and steady-state analysis. Each experimental run was conducted for 1 h, which was approximately five times the feed-side hydraulic residence time; it was determined from preliminary runs that this time period was sufficient to achieve steady-state. Since the main emphasis of the experiments was only to verify transient and steady-state CP behavior, all the experimental runs required 1 h to complete. The data were collected in intervals of 2 min for the first 20 min, and in intervals of 10 min for the remaining 40 min. Temperature was measured using an on-line temperature probe, and inlet and downstream operating pressures were measured using on-line pressure gauges. Feed, permeate and concentrate salt concentrations were measured employing a conductivity meter; this was relatively more convenient because a large number of samples were withdrawn for each run. Moreover, EC was linearly related to the salt concentration in the range of 0–0.1 M employed in this study. Four different feed NaCl concentrations (0.2, 0.5, 1.0 and 2.0 kg/m^3) in addition to pure water were used to study the effect of feed solute concentrations on CP and flux decline. In addition, two feed flow rates 1.28×10^{-4} and 1.91×10^{-4} m^3/s and three different recycle rates (recycle ratios R_c of 0.0, 0.5 and 1.0) were used to verify the effects of different cross-flow velocities. All the experiments were performed in the temperature range of 18–20°C.

4. Results and discussion

4.1. Parametric consistency

In order to verify the behavior of the model, a parametric study was undertaken. This included vary-

Table 2
Feed conditions, and membrane characteristics employed for (a) experimental verification and parametric analysis, and (b) accuracy analysis

Parameter	(a)	(b)
Membrane description		
Module type	Spiral wound RO	Spiral wound RO
Number of elements	3	1
Membrane characteristics		
Solute rejection (R)	0.98	0.98
Permeability A (20°C) (m/s KPa)	5.3×10^{-9}	7.45×10^{-9}
Channel width (2H) (m)	7.62×10^{-4}	8.0×10^{-4}
Length per element (m)	1.1	2.0
Area per element (m^2)	8.36	2.0
Operating conditions		
Ambient temperature (T_s) (°C)	20	25
Operating pressure (P) (KPa)	700–1250	3040
Flow regime	Laminar	Laminar
Feed Reynolds number (Re)	101	1333
Feed flow (Q_0) (m^3/s)	1.9×10^{-4}	6.0×10^{-4}
Initial inlet velocity (u_0) (m/s)	0.06	0.75
Fluid properties		
Feed solute concentration (c_0) (kg/m^3)	1.0	5.0
Solute diffusivity (D_s) (m^2/s)	1.61×10^{-9}	1.61×10^{-9}
Osmotic pressure constant (K_{osm}) (KPa m^3/kg)	75.4	68.9

ing A, R (solute rejection coefficient) and K_{osm} and ascertaining if the model behavior matched expected physical variations; for instance, increasing A effectively increased permeation rates and therefore increased CP. The feed and operating conditions for these tests are listed in Table 2. Fig. 4(a) and (b) show the effect of membrane permeability A on CP and loss in permeate flow. CP modulus, which is the ratio of the solute concentration calculated at the axial mid-point on the membrane surface at steady-state to the feed solute concentration, was plotted versus initial permeate recovery for various values of A. It was observed that the value of CP modulus steadily increased from $A=1.7\times10^{-9}$ to $A=6.8\times10^{-9}$ m/s KPa; this is expected since increasing A effectively increases permeation rate and therefore the transport of solute to the membrane surface. The effect of A on the reduction in overall permeate flow was also plotted to confirm this result. Steady-state values of permeate flow (in m^3/s) were plotted versus initial permeate flow; in the absence of CP, which is the case for pure water, it is expected that such a plot will be linear with a slope of unity i.e., there is no change in the permeate flow over time. However, the presence of solute results in CP and therefore the permeate flux decreases over time and eventually reaches a steady-state value that is lower than the starting flux. The overall decline is dependent on factors that aggravate CP; for instance, increasing A increases CP and causes a greater loss in permeate flow. This result is depicted in Fig. 4(b) where higher values of A cause the flux curves to bend towards the abscissa; conversely, lower values of A result in curves that linearly reflect low CP build-up.

Fig. 5(a) and (b) show the effect of solute rejection coefficient R and K_{osm} on CP. Rejection is defined as the percentage of the solute molecules retained on the feed side during membrane separation; from a physical viewpoint, decreasing R results in passage of solute molecules across the membrane barrier instead of accumulating near the surface. From Fig. 5(a), it can be observed that decreasing R from 98% to 60% results in lower values of CP modulus at the membrane surface which confirms the physical intuition. K_{osm} indicates the magnitude of osmotic pressure that is induced by a solute; increasing K_{osm} results in a

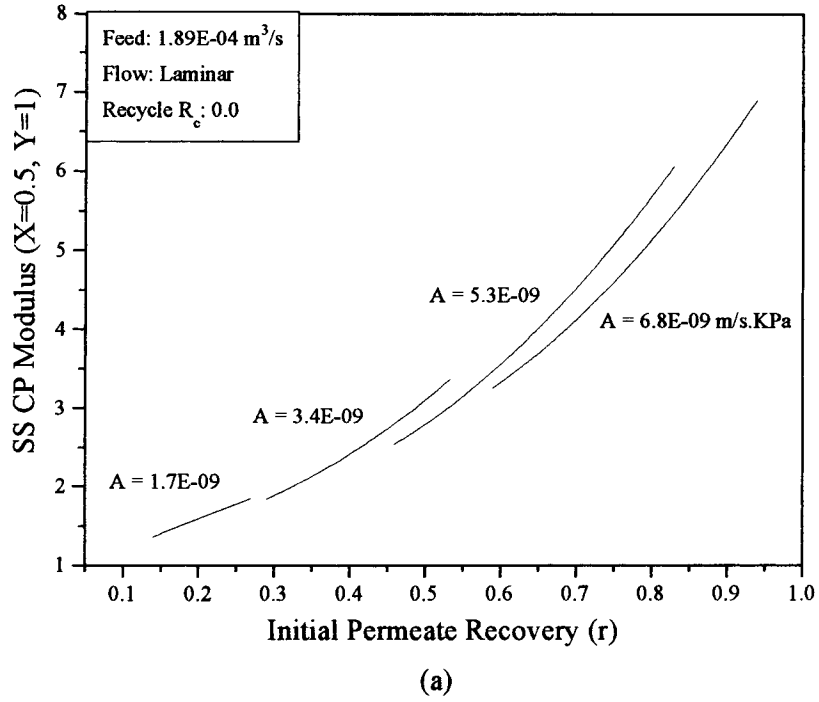

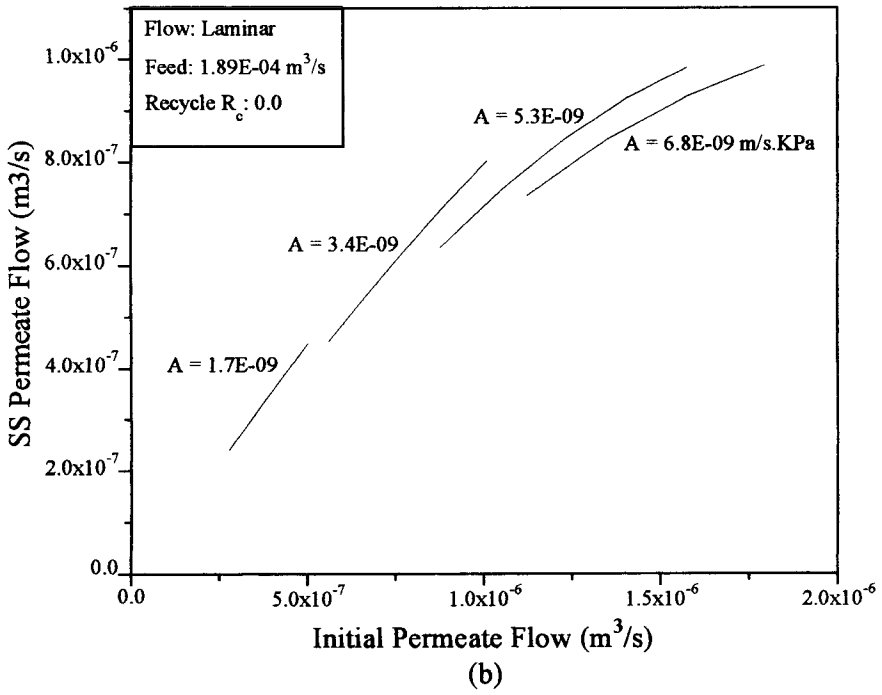

Fig. 4. Effect of membrane permeability A on: (a) steady state CP modulus, and (b) loss of permeate flow: initial flow plotted versus steady-state flow.

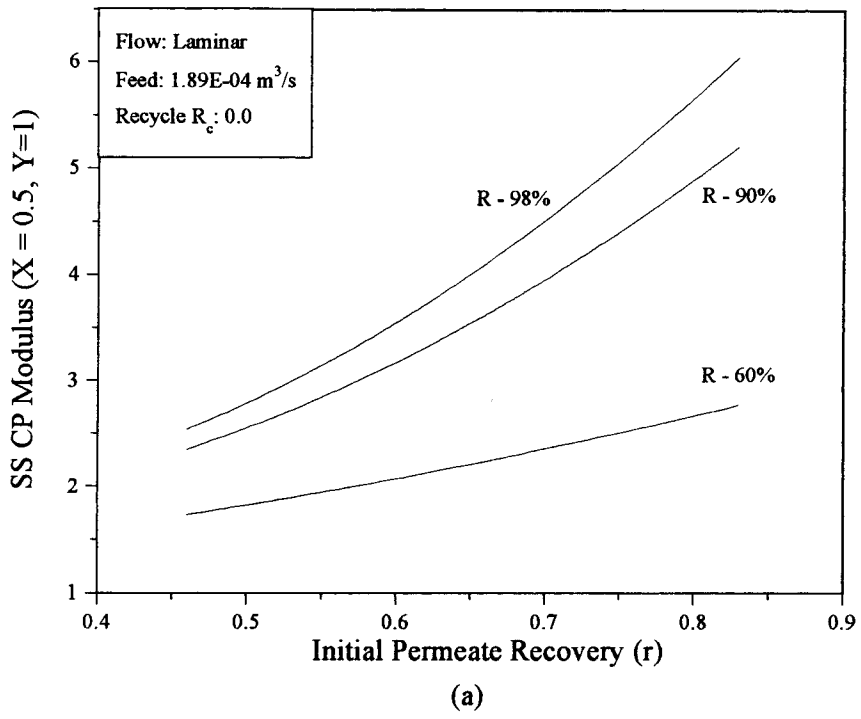

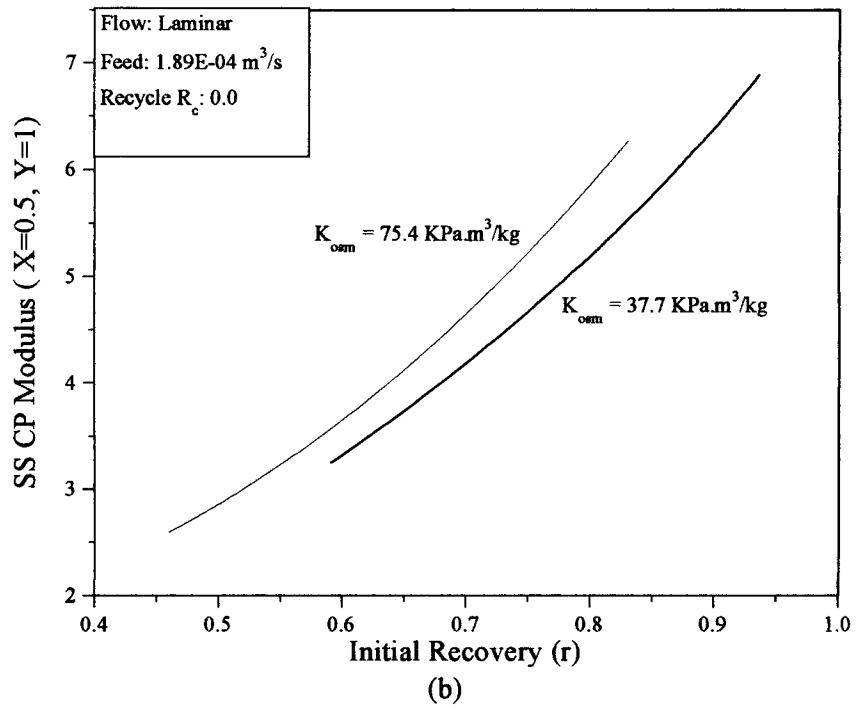

Fig. 5. (a) Effect of membrane rejection coefficient R on CP, and (b) effect of osmotic pressure constant K_{osm} on CP.

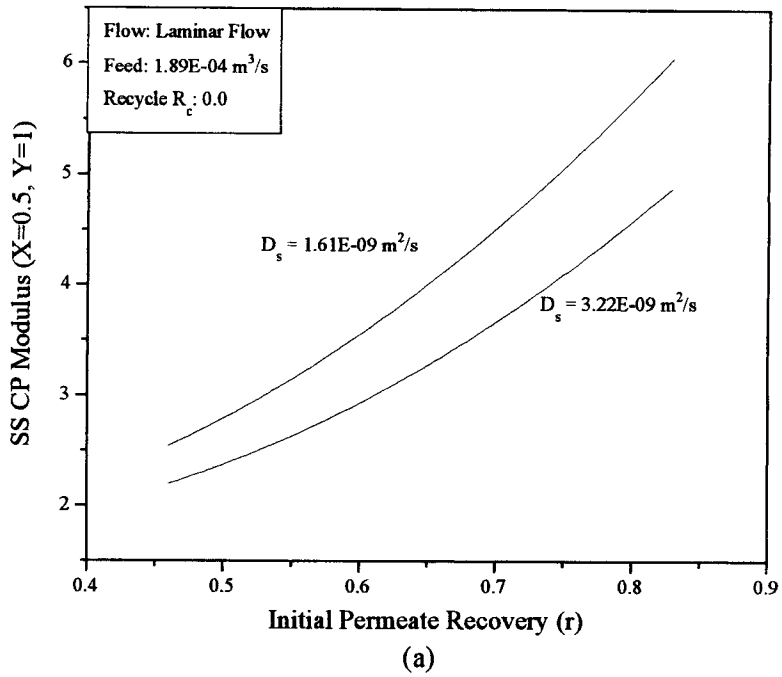

Fig. 6. Effect of solute diffusivity D_s on CP modulus.

high value of $\Delta\Pi$ and therefore an overall decrease in the solvent driving force $\Delta P-\Delta\Pi$. This translates to lower permeation rates and therefore lower CP. Two values of K_{osm} were chosen for ascertaining parametric consistency: $3.45\times10^{+3}$ and $6.89\times10^{+3}$ KPa m^3/kg. From Fig. 5(b), it can be observed that the lower K_{osm} value results in increased CP.

The model was also tested for parametric consistency with respect to D_s; however, D_s was used as a key parameter during scaling and thus an order of magnitude change altered the numerical stability of the problem, thus requiring different time and spatial increments. In order to minimize numerical discrepancies, the model runs were generated for two close Ds values: 1.61×10^{-9} m^2/s which is the molecular diffusivity of NaCl in water and 3.12×10^{-9} m^2/s which is twice the preceding value; the effect on CP is shown in Fig. 6. As expected, increasing D_s decreased CP because of increased solute back diffusion into the bulk stream.

The model was also tested for numerical accuracy by comparing with results of a steady-state CP model for commercial membranes. A steady-state CP model previously developed using an alternate solution technique namely a finite element formulation was chosen for comparison [10]. The operating conditions and membrane characteristics for this comparison are listed in Table 2, and the results are plotted in Fig. 7; it was found that the steady-state predictions of the transient model were within 10% of the predictions of the Bhattacharya model.

The model was also tested for numerical stability and for avoiding oscillatory problems. Though a von Neumann analysis was not conducted because of the complexities involved with the non-linear nature of the coefficients in the tri-diagonal coefficient matrix in Eq. (25), a relatively simpler analysis of the dependence of numerical solution on numerical grid size and time steps were undertaken. The numerical procedure was found to be conditionally stable in the lateral direction because of the parabolic nature of Eq. (9) in that direction. Accordingly, a relatively small time step of 1/200th of the nominal residence time was chosen. This ensured numerical stability in the lateral direction; Eq. (9) is hyperbolic in the axial direction, and therefore the adopted centered-difference procedure worked effectively.

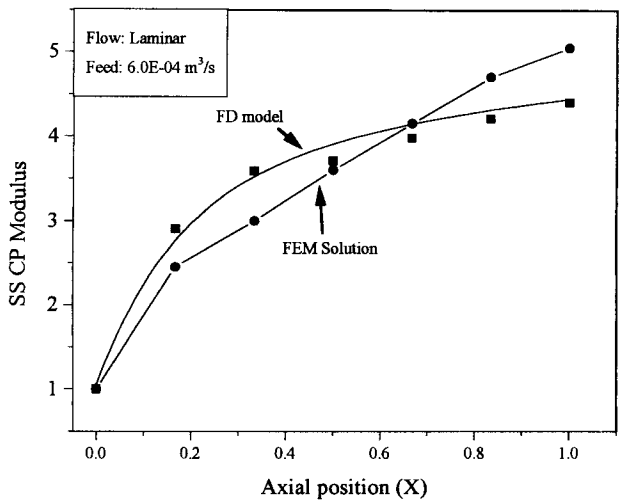

Fig. 7. Comparison of the CP results of the model with an earlier steady-state FEM solution [10]; operating conditions listed in Table 2.

4.2. Model predictions

Three different axial velocity profiles were used to duplicate laminar flow, completely mixed flow and spacer-induced mixing (partial mixing) regimes described by Eqs. (11), (14) and (15); some of the results were verified experimentally. Five feed solute concentrations were chosen for model runs at 0.01, 0.2, 0.5, 1.0 and 2.0 kg/m^3; four feed flow rates at 1.26×10^{-4}, 1.89×10^{-4}, 9.46×10^{-4}, 1.89×10^{-3} m^3/s and three recycle rates at recycle ratios of 0.0, 0.5, 1.0, 5.0 and 10 were chosen to investigate the effect of cross-flow. In addition, the effect of ambient temperature was also investigated at 15°C, 20°C and 25°C. Transient flux decline information that the model is capable of generating is illustrated for laminar flow for different feed concentrations in Fig. 8; the permeate fluxes are plotted as a function of time until steady-state conditions are attained. However, this procedure was not adopted for illustrating all model results. To conserve space, only steady-state results are shown for different feed and operating conditions, and flow regimes.

CP and loss in permeate flow are plotted for various feed concentrations in Fig. 9(a) and (b), respectively. Lower feed solute concentrations resulted in higher CP modulus values because of higher permeation rates. Since experiments were conducted only for salt concentrations ranging from 0.01 to 2.0 kg/m^3, the model predictions and discussion are limited to this range. The lower concentrations ranging up to 0.5 kg/m^3 reflect those found in typical municipal and industrial wastewater discharges while higher concentrations up to 2.0 kg/m^3 are more representative of brackish water sources. Laminar flow (Eq. (11)) results were also compared to completely-mixed flow regimes (Eq. (15)) for two feed concentrations: 0.01 and 1.0 kg/m^3; the latter invariably decreased CP and therefore the permeate flux decline because of more effective mass transfer via mixing (Fig. 10).

The effect of increasing cross-flow velocity was investigated in two ways: (1) increasing feed flow, and (2) increasing recycle flow. The effect of increasing feed flow on CP, and therefore permeate flux decline is shown in Fig. 11(a) while the effects of recycle flow rates are shown in Fig. 11(b). Two different flow rates were used to verify the model with experiments at 1.26×10^{-4} and 1.89×10^{-4} m^3/s (Reynolds Number – *Re* of 67 and 101, respectively); however, the model was also tested at flow rates of 9.46×10^{-4} and 1.89×10^{-3} m^3/s (*Re* values of 505 and 1010), and the results from this increase which are more dramatic, are shown in Fig. 11(a). As expected, higher feed flow rates directly reduced CP and permeate flow loss because of increased cross-flow and effective mass transfer. The impact of increasing recycle flow rates was more complicated because there were competing factors that influenced CP. The increase in cross-flow

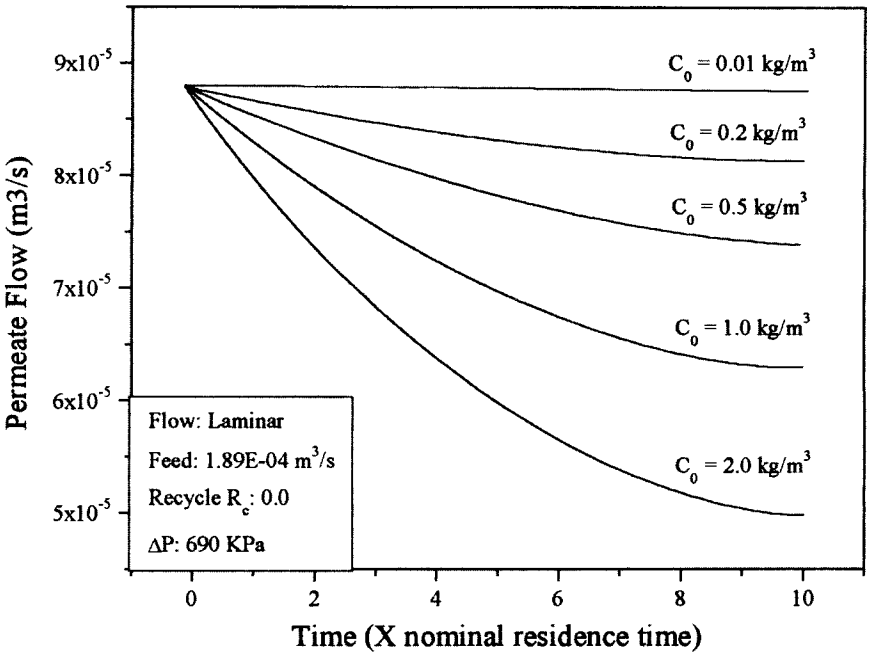

Fig. 8. Transient state model predictions: permeate flow loss is plotted versus time.

velocity had the impact of reducing CP and flux decline but it also contributed to an effective increase in feed concentration because of mixing with the more concentrated recycle fluid. While the latter effect was dominant at lower recycle rates (recycle ratios up to 1.0), CP was reduced at higher recycle flow rates (recycle ratios above 1.0). However, the results are only preliminary and need to be verified experimentally; this is especially important at higher cross-flow velocities because of the impact of axial pressure drop. In all the above model runs, a constant axial pressure drop of 10% was assumed; this could be higher in real systems leading to greater flux decline than what is shown in Fig. 11(b). The effect of temperature on permeate flux decline is illustrated in Fig. 12. Temperature was mainly assumed to influence A and K_{osm}. Since the permeability experiments on the membrane were conducted in the limited range of 15–25°C, the model runs were limited to this range. Nevertheless, increasing temperature had the effect of increasing permeability, and therefore increased CP and flux decline.

The model was also used to predict CP and loss in permeate flow for spiral wound membranes based on an axial velocity profile provided by Miyoshi (Eq. 76). The main parameter of interest was the constant m, which defined the extent of mixing induced by the spacer. Based on the specifications provided by the manufacturer in this study (Desal, based in Escondido, CA) on the spacer thickness (7.62×10^{-4} m), cross-bar thickness (2.16×10^{-4} m) and spacer porosity (at approximately 0.9), the constant was calculated to be 8.7 employing Eq. (8b). The losses in permeate flow for a specific feed concentration (0.5 kg/m^3) are compared with laminar and completely mixed flow ($m\rightarrow\infty$) regimes and plotted in Fig. 13(a). The laminar flow regime gave the highest CP and permeate flow loss confirming the need for effective solute mass transfer during membrane separation; the presence of the spacer only decreased CP and flux decline but the change was marginal. This result indicates the improvements that are necessary for increasing the effectiveness of the mixers by increasing m; for instance, decreasing spacer porosity considerably increases the value of m, ensuring adequate mixing.

The model was also used to study the effect of channel half-width H and the degree of mixing; the latter effect is represented by the parameter m. The

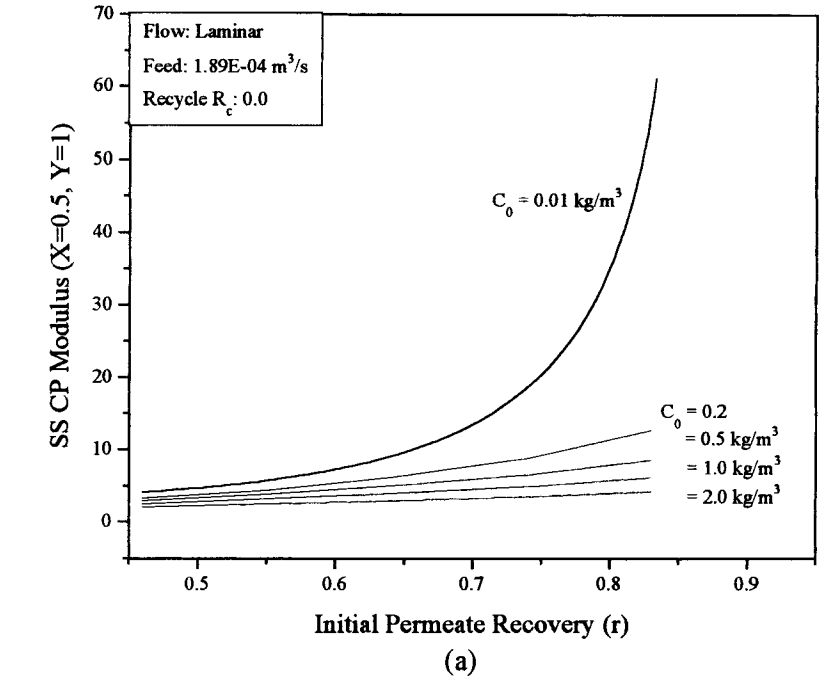

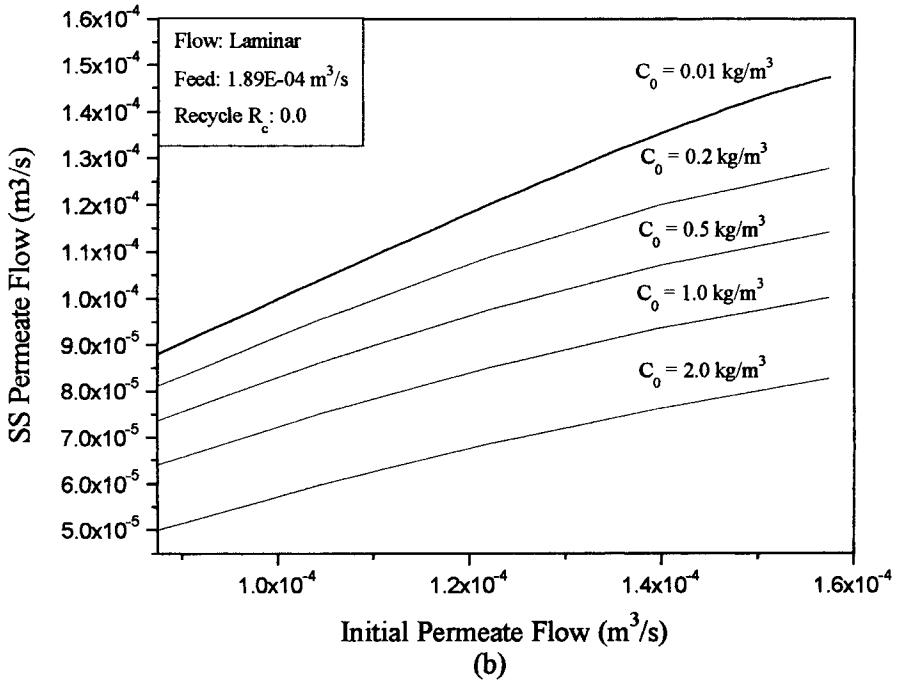

Fig. 9. Model predictions for various feed solute concentrations: (a) CP modulus versus recovery, and (b) initial versus steady-state permeate flow.

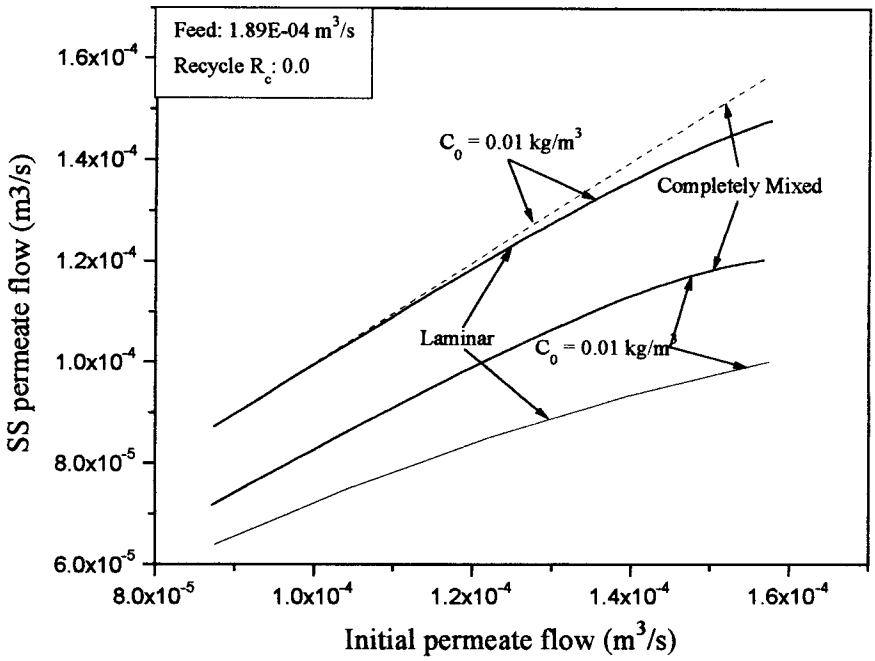

Fig. 10. Effect of laminar versus completely mixed flow regimes on permeate flow loss.

results on permeate flux decline for initial starting recovery of 0.83 are presented in Fig. 13(b); five values of H at 20, 25, 30, 35 and 40 mils (1 mil= 7.62×10^{-4} m), and four values of m at 1, 10, 100 and 1000 were chosen for model runs. The permeate flux decline was lowest for H value of 20 mils and m value of 1000; lower H values essentially increased cross-flow velocity while higher m values represented a greater degree of mixing and turbulence.

4.3. Experimental verification

The experimental data were compared with model runs for all the cases of axial velocity i.e., laminar flow, completely mixed flow and flow with feed spacers. Fig. 14(a) represents normalized flux decline data for a typical 1 h experiment conducted on the unit; for the feed flow rates used in these experiments (1.26×10^{-4}, 1.89×10^{-4} m^3/s), the 1 h test period was approximately 30 times the feed side fluid residence time. This test period was adequate for the permeate flux to decline to a steady-state value. The experimental flux values were adjusted for variations in the operating pressure since it varied, though within 10%, over the test period; this procedure facilitated comparison with model results where the operating pressure was assumed to be constant. From Fig. 14(a), it can be observed that there is approximately a 10% discrepancy between experimental flux decline and model predictions based on spacer-induced mixing; however, it was lower than the flux decline predicted by completely mixed flow. This difference is primarily attributed to two factors: (1) numerical error that is normally associated with any FD solution and/or (2) the limitations associated with the description of the eddy constant m. For instance in the latter case, the authors who provided expressions for the axial velocity ignored the effects of drag induced by the spacer in order to simplify analysis. In addition, empirical expressions were provided for m based on limited experiments conducted on standard spacers. Another discrepancy between experimental data and model predictions is the rate of development of CP and eventual flux decline; for instance, it can be observed from Fig. 14(a) that the flux decline in the case of experimental data is slower as compared to all the three model curves. This discrepancy is attributed to some of the basic assumptions associated with the

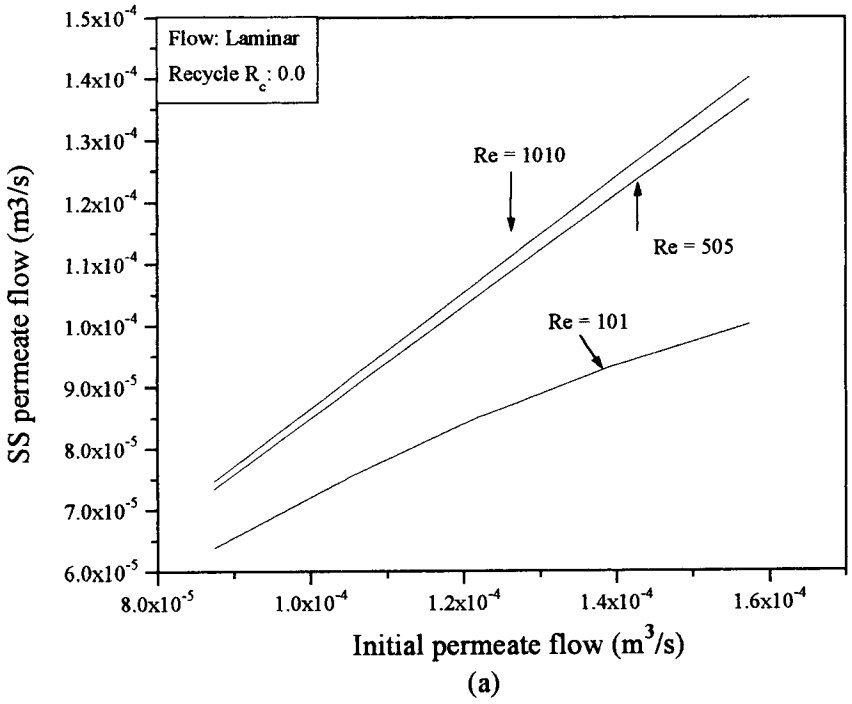

Fig. 11. Effect of cross-flow on CP and permeate flow loss: (a) *Re* versus flow loss, and (b) R_c versus flow loss.

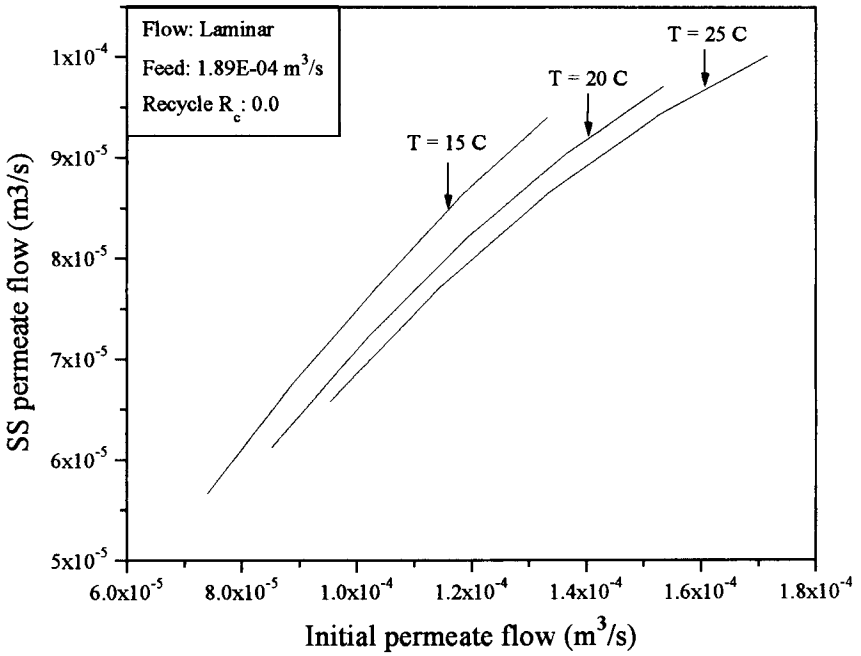

Fig. 12. Effect of ambient temperature on permeate flow loss at zero recycle.

model namely that the fluid is already at a steady-state on the feed side of the membrane before salt is introduced as a step function (i.e., from initial pure solvent to a specific feed concentration). However, this was not observed during the experiments because of the large quantity of pure solvent (water) that was necessary for each experiment. A typical experimental run consisted of operating the RO unit at a specific permeate recovery initially on 1.0 m^3 of clean water (with an approximate salt concentration of 0.01 kg/m^3) in a total recycle mode with both the concentrate and permeate being recycled to the feed tank. The RO unit was then suspended for a brief period of 2 min to mix a predetermined quantity of salt in the feed tank to attain a specific concentration, and restarted to conduct the flux decline experiment for that salt concentration. Thus, the procedure automatically insured that there was a delay in the build-up of CP and flux decline associated more with the positive displacement feed pump reaching its operating rpm. This discrepancy was limited to within two to three minutes of operation and did not affect flux decline thereafter. The steady-state values of CP modulus and flux decline that depended only on feed and operating conditions such as recovery, feed solute concentration and ambient temperature were also unaffected.

Steady-state data were compared with modeling results for various feed solute concentrations, operating pressures and recycle flow rates. In general, the modeling results based on laminar and spacer induced flow regimes consistently over-predicted permeate flow loss. However, flow loss based on completely mixed flow was consistently lower than that observed during the experiments. It is expected that model predictions based on laminar flow would over-predict permeate flow loss, while those based on completely mixed flow would under-predict it. This results because of the partial mixing, which is not described in either case. This was true in all the experiments that were conducted during this study. The relatively minor differences between experimental data and predictions based on spacer induced mixing can be attributed to the simplifying assumptions made during model development. Some of the steady-state results with respect to flow loss are shown in Fig. 14(b).

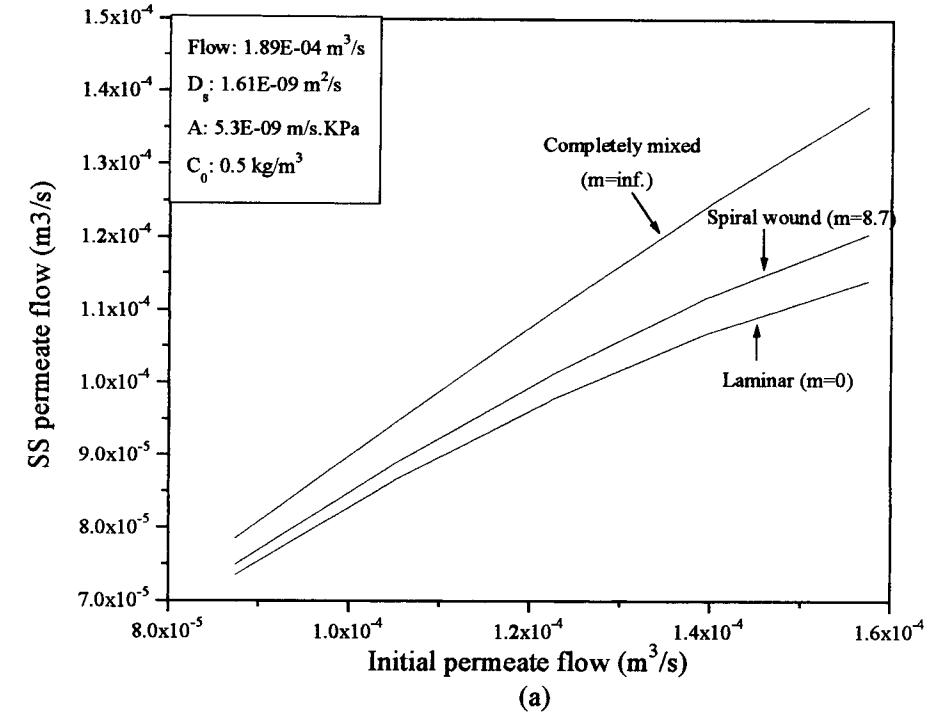

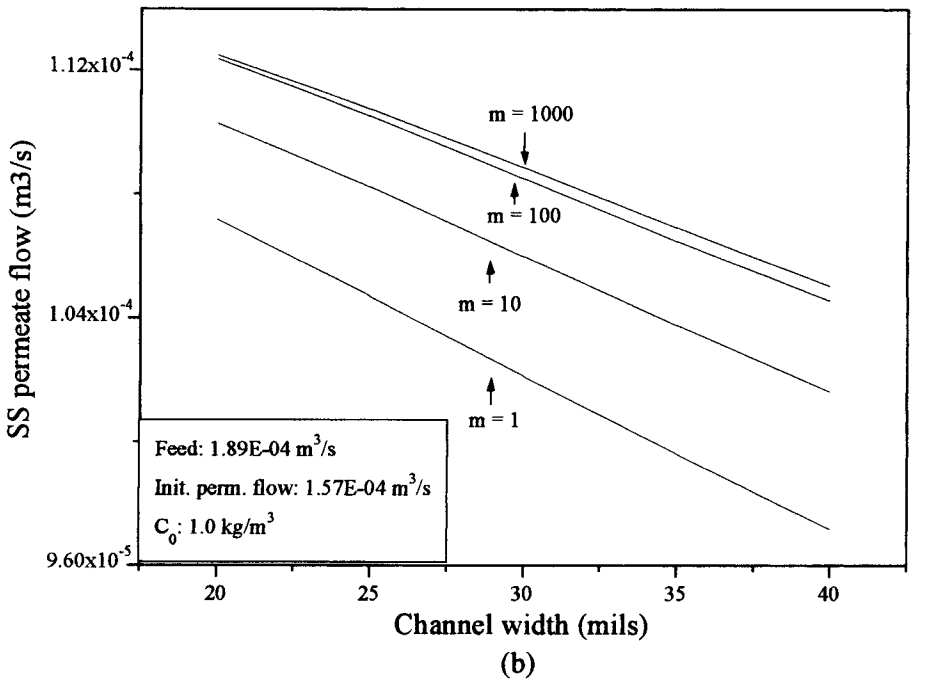

Fig. 13. Permeate flow loss at zero recycle plotted: (a) for various flow regimes, and (b) versus channel thickness in mils (1 mil=7.6×10^{-4} m) and mixing parameter m.

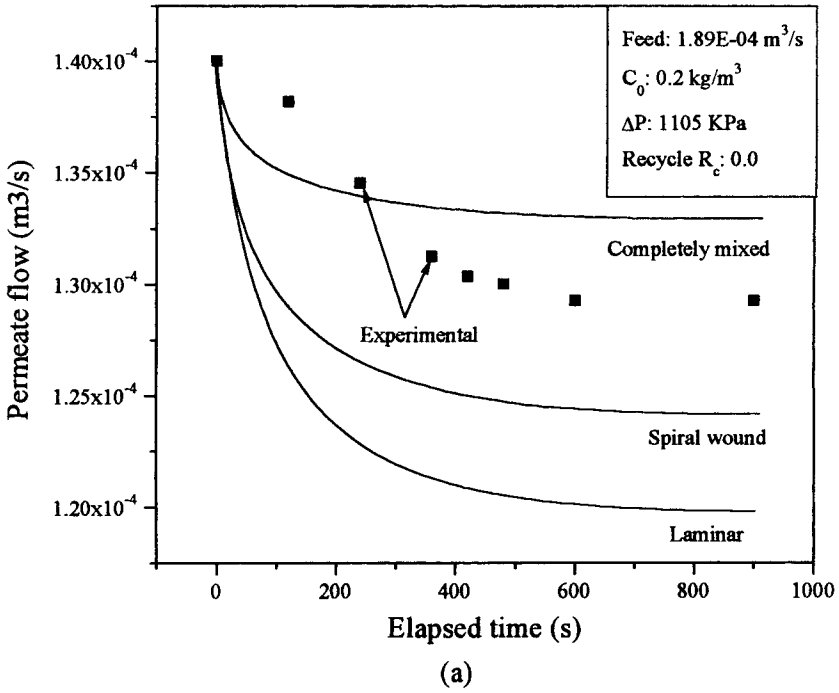

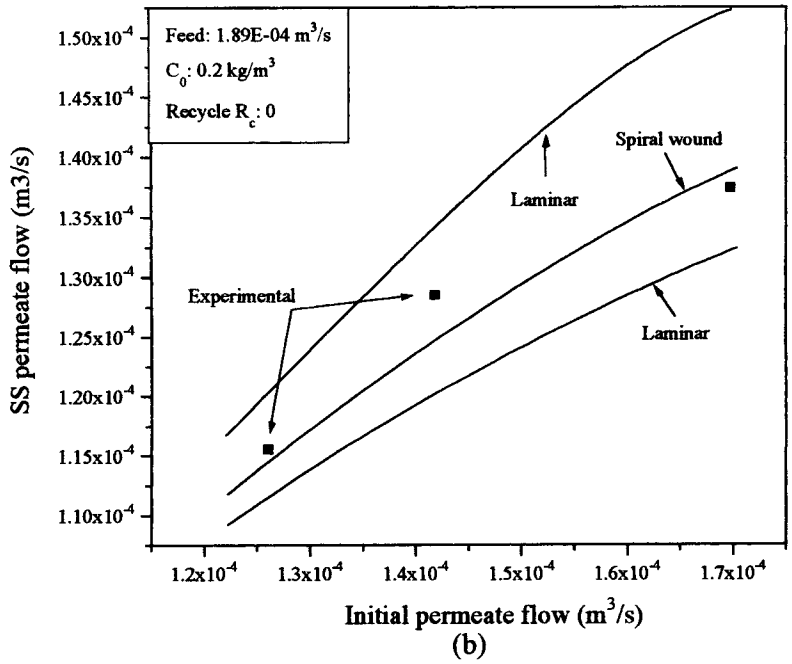

Fig. 14. Experimental verification on the pilot-scale RO unit: (a) transient-state data, and (b) steady-state data.

5. Summary and conclusions

Concentration polarization (CP) is a serious problem that has restricted the use of membranes. In this study, a transient state finite difference (FD) model for predicting CP and initial loss in permeate flow was developed and tested as a first step towards developing a more comprehensive model for long-term permeate flow loss in commercial membrane systems. A computer program was written to solve the solute mass balance equation along with the equations of fluid balance and continuity. The equations were written to describe flow in spiral wound membranes with feed spacers, but other flow regimes such as laminar flow and completely turbulent flow in rectangular channels were also analyzed. A wide range of feed and operating conditions were studied to ascertain the consistency and behavior of the model. The effect of other important membrane characteristics such as channel thickness, spacer characteristics and temperature were also studied. The effect of cross-flow was also studied by varying feed and recycle flow rates.

Experiments conducted on a pilot-scale spiral wound RO unit for separation of NaCl solutions at various feed concentrations, feed flow rates, recycle rates compared well with the model; the model consistently over-predicted permeate flow loss by approximately 10%. This was attributed to the limitations of the model, including numerical error as well as limitations relating to the description of the membrane, module and the spacers. For example, several assumptions were made during the formulation of the model such as constant solute rejection, constant axial pressure drop of 10% on all model runs and the absence of spiraling effects. Nevertheless, the model was successful in accurately predicting the effects of CP and is expected to be useful in the design of commercial membrane systems. The overall formulation of the model is also relatively easy to interpret, and is therefore expected to be useful for separation problems involving colloidal and organic matter removal that are described by other membrane flux models such as the gel polarization model or the resistances model. Another advantage of the model is its relevance to long-term flux decline; as each model runs reaches steady-state with respect to CP, progressively larger time increments can be taken in order to incorporate these effects. Thus, a substantial amount of flux decline information could be generated within reasonable computation times.

6. Nomenclature

A	membrane permeability (m/s KPa)
c	solute concentration (kg/m^3)
c_0	inlet (feed) solute concentration
C	scaled solute concentration ($C=c/c_0$)
C_p	scaled permeate solute concentration
C_R	scaled recycle solute concentration
C_w	scaled wall solute concentration
d_s	spacer fiber thickness
D	scaled solute diffusivity ($D_s L/u_0 H^2$)
D_s	solute diffusivity (m^2/s)
$2H$	channel thickness (m)
K_{osm}	osmotic coefficient (KPa m^3/kg)
i	numerical variable in x-direction
j	numerical variable in y-direction
L	channel axial length (m)
m	mixing parameter
n	numerical variable in time
n_s	number of spacers
P	applied pressure on the feed side (KPa)
ΔP_{ax}	axial pressure drop (KPa)
R	percent rejection coefficient (100 ($C-C_p$))
R_c	recycle ratio
Re	axial Reynolds number ($4H u_0/\nu$)
t	time coordinate (s)
t_s	spacer thickness
T	scaled time coordinate ($t u_0/L$)
u	axial velocity (m/s)
u_0	axial velocity at the module inlet
U	scaled axial velocity (u/u_0)
U_{avg}	space-averaged scaled axial velocity
v	lateral velocity (m/s)
v_w	wall permeation velocity
V	scaled lateral velocity ($\nu L/u_0 H$)
V_p	scaled permeation velocity
V_w	scaled wall permeation velocity
x	axial coordinate (m)
X	scaled axial coordinate (x/L)
y	lateral coordinate (m)
Y	scaled lateral coordinate (y/H)

Greek letters

ϵ spacer porosity
ν solvent kinematic viscosity (m^2/s)
Π osmotic pressure (KPa)
ρ solvent density (kg/m^3)

Acknowledgements

The authors are grateful to the Ahmanson Foundation that funded this research and the Lake Arrowhead pilot-study. They are especially thankful to the Lake Arrowhead Community Services District (LACSD), and Mr. Ken Nelsen, the chief operator at their wastewater treatment facilities. They are also grateful to the many graduate students at the University of California, Los Angeles, who participated in this study.

References

[1] T. Liu, The application of membranes in environmental protection, Desalination 62 (1987) 149–164.
[2] M.R. Weisner, J. Hackney, S. Sethi, G. Jacangelo, J.M. Laine, Cost estimates for membrane filtration and conventional treatment., J. Am. Water Works Association 86 (1994) 33–41.
[3] G. Belfort, Synthetic Membrane Processes, Academic Press, Orlando, FL, 1984.
[4] D.E. Potts, R.C. Ahlert, S.S. Wang, A critical review of fouling of reverse osmosis membranes, Desalination 36 (1981) 235–264.
[5] C.R. Bouchard, P.J. Carreau, T. Matsuura, S. Sourirajan, Modeling of ultrafiltration: prediction of concentration polarization effects, J. Membr. Sci. 97 (1994) 215–229.
[6] H. Miyoshi, T. Fukuumoto, T. Kataoka, A consideration of flow distribution in an ion exchange compartment with spacer, Desalination 42 (1982) 47.
[7] J.D. Hoffman, Numerical Methods for Engineers and Scientist, McGraw-Hill, New York, 1992.
[8] S. Sourirajan, Reverse Osmosis, Appendix A-16 and 17, Academic Press, New York, 1970.
[9] K. Madireddi, R.W. Babcock, B. Levine, T.L. Huo, E. Khan, Q.F. Ye, J.B. Neethling, I.H. Suffet, M.K. Stenstrom, Wastewater reclamation at Lake Arrow-head California: an overview, Water Environ. Res. 69 (1997) 350.
[10] D. Bhattacharya, S.L. Back, R.I. Kermode, Prediction of concentration polarization and flux behavior in reverse osmosis by numerical analysis, J. Membr. Sci. 48 (1990) 231–262.
[11] A.S. Berman, Laminar flow in channels with porous walls, J. Appl. Phys. 24 (1953) 1232–1235.